

Instability of Non-uniform Toroidal Magnetic Fields in Accretion Disks

Kota Hirabayashi and Masahiro Hoshino

*Department of Earth and Planetary Science, The University of Tokyo, 7-3-1, Hongo, Bunkyo-ku,
Tokyo 113-0033, Japan*

hirabayashi-k@eps.s.u-tokyo.ac.jp

ABSTRACT

A new type of instability that is expected to drive magnetohydrodynamic (MHD) turbulence from a purely toroidal magnetic field in an accretion disk is presented. It is already known that in a differentially rotating system, the uniform toroidal magnetic field is unstable due to a magnetorotational instability (MRI) under a non-axisymmetric and vertical perturbation, while it is stable under a purely vertical perturbation. Contrary to the previous study, this paper proposes an unstable mode completely confined to the equatorial plane, driven by the expansive nature of the magnetic pressure gradient force under a non-uniform toroidal field. The basic nature of this growing eigenmode, to which we give a name “magneto-gradient driven instability”, is studied using linear analysis, and the corresponding nonlinear evolution is then investigated using two-dimensional ideal MHD simulations. Although a single localized magnetic field channel alone cannot provide sufficient Maxwell stress to contribute significantly to the angular momentum transport, we find that the mode coupling between neighboring toroidal fields under multiple localized magnetic field channels drastically generates a highly turbulent state and leads to the enhanced transport of angular momentum, comparable to the efficiency seen in previous studies on MRIs. This horizontally confined mode may play an important role in the saturation of an MRI through complementray growth with the toroidal MHDs and coupling with magnetic reconnection.

Subject headings: accretion, accretion disks — instabilities — magnetohydrodynamics — methods: numerical — turbulence

1. INTRODUCTION

Accretion disks are one of the most ubiquitous astrophysical objects, comprising dynamics such as astrophysical jets, disk winds, and particle acceleration. It is widely believed that these dynamical phenomena are driven by the anomalous transport of angular momentum and the subsequent release of gravitational binding energy. Several mechanisms have been proposed in attempts to explain the origin of this angular momentum transport. Examples include magnetic braking

by external, large-scale magnetic fields (e.g., Blandford & Payne 1982; Stone & Norman 1994), non-axisymmetric wave excitation (e.g., Fragile & Blaes 2008), and hydrodynamic/hydromagnetic turbulence (e.g., Papaloizou & Pringle 1984; Balbus & Hawley 1998). In this paper, we consider a mechanism related to the third example, which is the sole candidate that possesses a high correlation with conventional, α -disk models (Shakura & Sunyaev 1973). In the α -disk models, the efficiency of angular momentum transport, which is determined by the $R\phi$ -component of the stress tensor, is determined as the product of the pressure and a given parameter α . The value of α depends significantly on viscosity physics, but the simple molecular viscosity in an accretion disk cannot provide a high efficiency of angular momentum transport suggested by observations (Cannizzo et al. 1988). Since the astrophysical importance of magnetorotational instability (MRI) as the origin of required turbulence was pointed out (Balbus & Hawley 1991, 1998), a number of authors have investigated the nature of MRIs and the resultant turbulence in accretion disks over a wide range of plasma parameters (e.g., Stone et al. 1996; Sano & Stone 2002; Kunz & Lesur 2013; Hoshino 2015; Bai 2015; Zhu et al. 2015; Simon & Hawley 2009; Simon et al. 2012).

In order to study the basic behavior behind the non-linear time evolution of MRIs, most numerical studies on the local properties of MRI-induced turbulence have adopted the shearing box model (Hawley et al. 1995; Sano & Inutsuka 2001; Sharma et al. 2006), which can capture the wave vector toward an arbitrary direction in a differentially rotating plasma. Since an MRI with a vertical wave vector has the maximum growth rate for an axisymmetric perturbation when the background magnetic field is purely poloidal, fully three-dimensional simulations, or at least two-dimensional ones including a vertical axis, are necessary. (Note that the final states in two- and three-dimensional cases are rather different from each other, and that the three-dimensional simulations are required to investigate the saturation stage.)

The situation is similar when the unperturbed magnetic field is purely toroidal. For example, Balbus & Hawley (1992) investigated the linear stability of an accretion disk threaded by a uniform toroidal magnetic field assuming three-dimensional wavevectors in the cylindrical coordinates, whose x -component varies with time because of the background shear velocity. They showed that the perturbation satisfying $\mathbf{k} \cdot \mathbf{V}_A \lesssim \Omega$ can become unstable, in the sense that the amplitude of oscillation increases with time. Moreover, a finite vertical wavenumber, k_z , is required for the instability to occur, and the larger k_z leads to the faster amplification. The non-linear evolution of this oscillatory instability was also examined by Hawley et al. (1995) using three-dimensional ideal MHD simulations, and the contribution to turbulence generation was confirmed.

Other examples include linear eigenvalue analyses and the corresponding MHD simulations by Matsumoto & Tajima (1995). They revealed that purely growing eigenmodes can exist in a shearing plasma, in contrast to the above oscillatory unstable modes. For a Keplerian disk, only the non-axisymmetric perturbations with $k_y^2/k_z^2 < 0.015$ become purely growing modes, where k_y and k_z are the azimuthal and vertical wavenumbers, respectively. The vertical waves, therefore, again contribute to the unstable modes most significantly, although a finite azimuthal wavenumber is required.

Such a situation, where the toroidal magnetic field is dominant, is thought to appear easily in the non-linear stage of an MRI even when starting from a poloidal field. For understanding the dynamics and the nature of turbulence in well-developed disks, therefore, it is important to investigate a plasma stability under a purely toroidal field. In this paper, we provide the results of linear and non-linear analyses on this issue, focusing particularly on an initially non-uniform toroidal field, and suggest another possible path leading to turbulence generation. Unstable modes proposed here, which we will call “magneto-gradient driven instability (MGDI)” reflecting its driving source as shown in the succeeding sections, are confined within the equatorial plane, i.e., $k_z = 0$, in contrast to the previous studies that required $k_z^2 > k_y^2$. An instability bound to the equatorial plane may play a crucial role in plasma transport, as it could potentially couple with magnetic reconnection occurring in the plane and contribute to the saturation mechanism of MRIs.

The outline of this paper is as follows. In Section 2, we briefly introduce the setup of our theoretical study and show the existence of unstable eigenmodes by linear analysis. Section 3 discusses the results of the fully-non-linear two-dimensional numerical simulations. The non-linear calculations corresponding to the linear study and ones which can lead to more turbulent states are presented. Finally, Section 4 is devoted to the summary and conclusion of our results.

2. LINEAR ANALYSIS

In this section we investigate the linear stability of a non-uniform toroidal magnetic field in a differentially rotating system. In particular, a simplified situation with a localized toroidal magnetic field channel is considered to extract the physical essence of possible unstable modes.

2.1. Equilibrium State and Linearized Equations

The ideal MHD equations incorporated with the standard shearing box model are employed as the basic equations throughout this paper (Stone & Gardiner 2010):

$$\frac{\partial \rho}{\partial t} + \mathbf{v} \cdot \nabla \rho = -\rho \nabla \cdot \mathbf{v}, \quad (1)$$

$$\rho \left(\frac{\partial \mathbf{v}}{\partial t} + \mathbf{v} \cdot \nabla \mathbf{v} \right) = -\nabla \left(p + \frac{B^2}{2} \right) + \mathbf{B} \cdot \nabla \mathbf{B} - 2\rho \boldsymbol{\Omega} \times \mathbf{v} - 2\rho \Omega x v'_{y0} \hat{\mathbf{e}}_x, \quad (2)$$

$$\frac{\partial \mathbf{B}}{\partial t} = \nabla \times (\mathbf{v} \times \mathbf{B}), \quad (3)$$

$$\frac{\partial p}{\partial t} + \mathbf{v} \cdot \nabla p = -\gamma p \nabla \cdot \mathbf{v}. \quad (4)$$

The radial and azimuthal directions are then interpreted as the x - and y -axes in the local Cartesian coordinate system, where the differential rotation is described by a linearly changing background velocity defined as $v_{y0}(x) = -q\Omega x$, using an angular velocity at the center of the computational

domain, Ω , and a positive constant, q . The specific heat ratio, γ , is set to be 5/3, and the other notations are standard.

When a purely toroidal magnetic field is imposed, the background shearing plasma is kept in an equilibrium state as long as the total pressure is spatially constant. We can, therefore, choose an arbitrary magnetic structure with a finite gradient. Here, we focus on the idealized case with a simple localized toroidal field,

$$B_{y0}(x) = B_0 \cosh^{-2}(x/d), \quad (5)$$

where B_0 is the field strength at $x = 0$ and d is the typical width of the localized field. The gas pressure is determined so as to satisfy the total pressure balance, and the background density is distributed so as to keep the temperature uniform.

Next, we linearize the MHD equations around this equilibrium state, assuming the functional form of a small perturbation as

$$f_1(x, y, t) = f_1(x) \exp(-i\omega t + ik_y y). \quad (6)$$

The vertical dependence is ignored so as to pick up horizontally confined modes. Using the vector potential instead of the magnetic field, the linearization of the basic equations leads to the following eigenvalue problem:

$$\omega \mathbf{U}_1 = \mathbf{M} \mathbf{U}_1, \quad (7)$$

where $\mathbf{U}_1 = (v_{x1} \ v_{y1} \ A_{z1} \ p_1)^T$ is a first-order perturbation vector, and \mathbf{M} is a coefficient matrix whose components are given as follows,

$$\begin{aligned} \mathbf{M} &= k_y v_{y0} \mathbf{I} + \mathbf{D}, \\ \mathbf{D} &= \begin{pmatrix} 0 & 2i\Omega & D_{13} & -(i/\rho_0) \partial_x \\ D_{21} & 0 & -k_y B'_{y0}/\rho_0 & k_y/\rho_0 \\ iB_{y0} & 0 & 0 & 0 \\ D_{41} & \gamma k_y p_0 & 0 & 0 \end{pmatrix}, \\ D_{13} &= (i/\rho_0) [B_{y0} (\partial_x^2 - k_y^2) + B'_{y0} \partial_x], \\ D_{21} &= -iv'_{y0} - 2i\Omega, \\ D_{41} &= -ip'_0 - i\gamma p_0 \partial_x. \end{aligned}$$

Here, \mathbf{I} is the identity matrix, and ∂_x and \cdot' indicate differentiation operators by x . Note that the equations for v_{z1} and B_{z1} are decoupled as usual shear Alfvén waves. Although the density perturbation, ρ_1 , appears to have disappeared from the basic equations, compressional modes remain in the system and ρ_1 can be obtained from $\nabla \cdot \mathbf{v}_1$.

Finally, equation (7) is discretized in the computational domain $|x/L_x| \leq 1$ with 400 grid points using a fourth-order central difference. The width of the localized field is set to be $d = 0.05L_x$. As a boundary condition, a conducting wall is assumed at $|x/L_x| = 1$. The eigenvalues, ω , and the eigenvectors, \mathbf{U}_1 , are then computed numerically.

2.2. Growth Rates

From our calculations of the eigenvalue problem described above, we obtained one growing mode for the MGDI at most for each particular wavenumber value. The results are summarized in Figure 1, where the color contour shows the imaginary parts of the eigenvalues as a function of the wavenumber, normalized by the width of the localized field, and the plasma beta, $\beta = 2p/B^2$, measured at $x = 0$. Note that the real parts are zero in a machine precision.

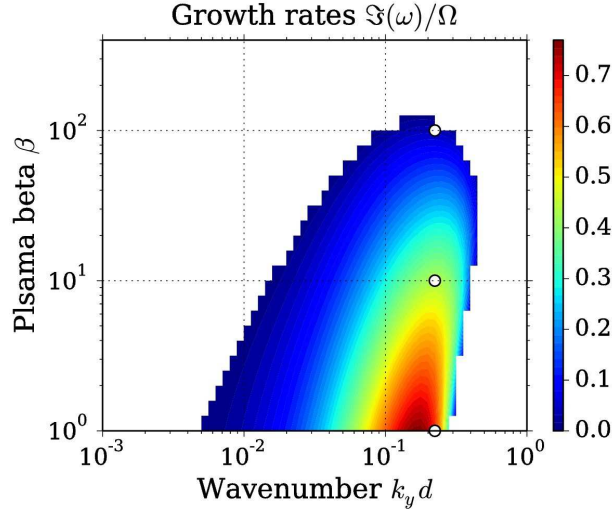


Fig. 1.— The color contour of growth rates as a function of the plasma beta and the wavenumber normalized by d , which is the width of the localized toroidal field. The gradient of the angular velocity, q , is set to unity.

Figure 1 indicates that the purely growing mode appears if β is lower than about 100, and that the growth rate becomes larger as the initial magnetic field strength increases. When β is equal to unity, the maximum growth rate reaches 0.765Ω , which is comparable to that of the axisymmetric MRI, i.e., 0.75Ω , as far as the linear approximation is appropriate. We should emphasize here that the magnitude of the velocity shear, q , is assumed to be unity in Figure 1 for theoretical simplicity, which is smaller than in the case of Keplerian rotation, where $q = 1.5$. In the Keplerian rotation case, we expect more unstable eigenmodes due to the stronger shear motion.

A physical picture of the MGDI can be explained as follows. Let us consider an outward going perturbation in v_{x1} away from $x = 0$, i.e., positive for $x > 0$ and negative for $x < 0$. Since a linearized equation for the azimuthal magnetic field can be written as

$$\frac{dB_{1y}}{dt} = -B_{y0}\frac{\partial v_{x1}}{\partial x} - B'_{y1}v_{x1} - q\Omega B_{x1}, \quad (8)$$

where $d/dt = \partial/\partial t + \mathbf{v}_0 \cdot \nabla$ is a Lagrangian derivative, such outward v_{x1} directly induces the increment in B_{y1} through the second term in the right-hand side. This term comes from the

linearized advection effect, which represents the fact that a fluid element brings the frozen-in magnetic field line from the original position with the stronger magnetic field. On the other hand, a linearized version of the equation of motion for the radial velocity is as follows,

$$\rho_0 \frac{dv_{x1}}{dt} = -\frac{\partial p_1}{\partial x} - \frac{\partial}{\partial x} (B_{y0} B_{y1}) + B_{y0} \frac{\partial B_{x1}}{\partial y} + 2\rho_0 \Omega v_{y1}. \quad (9)$$

The second and third terms in the right-hand side represent the magnetic pressure gradient and the magnetic tension force, respectively. The magnetic pressure can be further decomposed into two contributions from $-B'_{y0} B_{y1}$ and $-B_{y0} \partial_x B_{y1}$. The increase in B_{y1} , then, leads to further expansion force via the first component of the magnetic pressure, which implies a positive feedback. This feedback process will continue to work as long as the finite gradient in the background magnetic field is available.

As well as the growth rates, the range of unstable wavenumbers also tends to broaden as the plasma beta decreases, especially toward the long-wavelength side. The smallest scale, on the other hand, seems to always be limited roughly by $k_y d < 0.5$, which corresponds to the wavelength one order of magnitude larger than d . This bound could be understood qualitatively by the competition between the magnetic pressure gradient force, which is a driver here, and the magnetic tension force working as a restoring force. For the feedback mechanism described above to occur, it is clear that the expansive nature of the magnetic pressure needs to be greater than the tension effect. These promoting and restoring effects can be rearranged into the form of the Lorentz force, $\mathbf{J}_1 \times \mathbf{B}_0$ and $\mathbf{J}_0 \times \mathbf{B}_1$. The schematic view of the situation is illustrated in Fig.2. Then the condition that the expansive term outpaces the restoring force is roughly estimated as

$$\left| \frac{\partial B_{y0}}{\partial x} B_{y1} \right| > \left| \frac{\partial B_{x1}}{\partial y} B_{y0} \right|.$$

Replacing the derivatives by typical scales like $1/d$ and k_y , we obtain the estimate, $1/d > k_y$, which is consistent with the unstable range in Figure 1.

The destabilization mechanism described above seems not to be related to the nature of the differential rotation. For the purpose of comparison, growth rates in a rigid-rotating plasma are shown in Figure 3 with the same format as in Figure 1. This panel indicates the existence of unstable modes over a similar range to that in the differentially-rotating case. The qualitative dependence on k_y and β also resembles that in Figure 1, but the magnitude of the growth rate becomes smaller by a factor of 2 for $\beta = 1$, and much more for larger β . Therefore, it can be concluded that this instability arises originally from the gradient of the magnetic field, and can attain a large growth rate comparable to that of the standard MRI only when combined with the shearing motion.

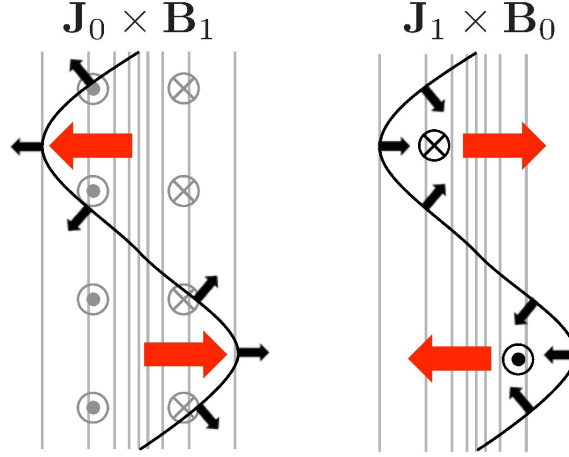


Fig. 2.— Schematic view of first-order Lorentz forces. In the left panel, the background current (\mathbf{J}_0 ; gray circles) makes expansive Lorentz force (black arrows) combined with the perturbed magnetic field (\mathbf{B}_1 ; black lines). The resultant force works to increase the perturbation, like shown by the red arrows. In the right panel, on the other hand, a cross product of the first-order current (\mathbf{J}_1 ; black circles), which is generated by the perturbed magnetic field, and the background magnetic field (\mathbf{B}_0 ; gray lines) makes the inward Lorentz force, which always works as the restoring force.

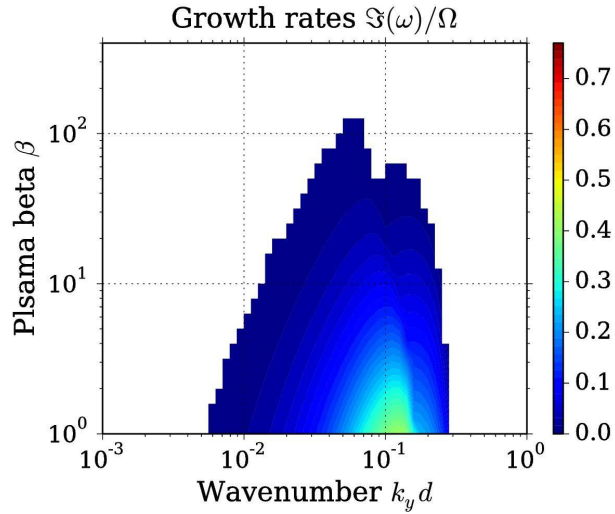


Fig. 3.— The color contour of growth rates in a rigid-rotating plasma, $q = 0$, with the same format as in Figure 1.

2.3. Eigenfunctions

Let us discuss the structure of the eigenfunctions. Figure 4 shows two-dimensional representations of the Fourier decomposed eigenfunction, \mathbf{U}_1 , superposed on the background equilibrium state, \mathbf{U}_0 , where \mathbf{U}_1 is normalized to satisfy $|\mathbf{U}_1| = 1$. Based on the normalized case in panel (b), the states before and after twice the e -folding time are shown in panels (a) and (c), respectively. The plasma beta and the wavenumber are chosen to be $\beta = 100$ and $k_y d = 0.223$, respectively, and the corresponding point on the k_y - β diagram is plotted in Figure 1 by an outlined circle. In each panel, the color contour, the solid lines, and the vector field show the gas pressure distribution, the lines of magnetic force, and the bulk velocity, respectively.

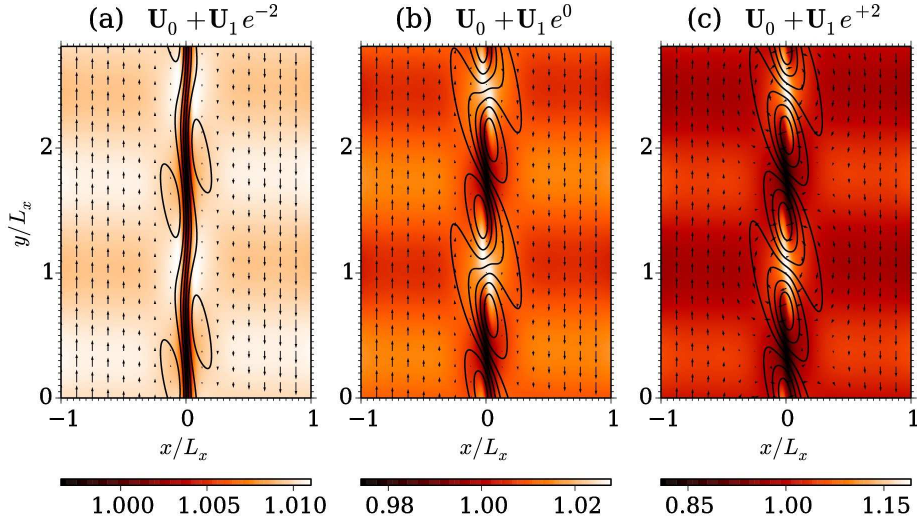


Fig. 4.— Two-dimensional views of an unstable eigenfunction with the wavenumber $k_y d = 0.223$, superposed on the background plasma with $\beta = 100$. The corresponding growth rate is 0.039Ω . The color contour, the solid lines, and the vector map indicate the gas pressure, the magnetic field lines, and the velocity, respectively. The first-order eigenfunction \mathbf{U}_1 is normalized by $|\mathbf{U}_1| = 1$. From left to right, the amplitude of the eigenfunction increases $2e$ -fold.

Figure 4 shows that bending of the field line broadens with time, and eventually spreads out beyond the typical width of the equilibrium field, $d = 0.05L_x$. This broadening of the field line is explained by the destabilization process described in the previous subsection, i.e., the outward magnetic pressure gradient exceeding the inward magnetic tension force may further expand the magnetic field explosively. In addition to the expansion in the x -direction, the field lines are also stretched in the y -direction by the so-called Ω -effect due to the background shear motion, and thus the magnetic field lines become inclined downward to the right. In other words, B_x and B_y tend to have negative correlation. Therefore, it can be expected that the MGDIs have the

potential to contribute to powerful angular momentum transport, making the averaged Maxwell stress, $\langle -B_x B_y \rangle$, once developing to non-linear turbulence.

Other important features include vortex structures around the nodes of the magnetic field lines in panel (c). In particular, the clockwise vortices at every other node, which align with the differential rotation, are selectively enhanced. Since the Coriolis force works rightward to the direction of motion, the inside of the clockwise vortex is compressed, and the other is expanded. On the other hand, the selective enhancement makes the magnetic field lines loosened around the clockwise vortex, as if a tightly stretched rope is reeled up. This leads to the negative correlation between the gas pressure and the magnetic pressure, which implies that the present unstable mode essentially arises from slow-magnetosonic waves.

Looking at Figure 4, one may associate the MGDIs with current-driven instabilities (CDIs), which are thought to contribute fast dissipation of magnetic energy in various astrophysical contexts (e.g., Mignone et al. 2010; O’Neill et al. 2012; Mizuno et al. 2014). Although the characteristic that both unstable modes are driven by magnetic non-uniformity is common, we consider the MGDI as a fundamentally different mode from the CDI. To make the difference clear, for example, notice that the wavevector in the CDI is essentially parallel to the background electric current, which drives the instability. In the case of the MGDI, on the other hand, the background current has only an out-of-plane component, which is obviously perpendicular to wavevector of the perturbation.

Figures 5 and 6 show the eigenfunctions for the cases with $\beta=10$ and 1, respectively, in the same format as in Figure 4. The wavenumber is again assumed to be $k_y d=0.223$. Since the magnetic tension force, working as a restoring force, becomes stronger with an increase in the magnetic field strength, it becomes more and more difficult to bend the magnetic field lines significantly, and the unstable mode seems to be localized around the initial localized channel. It should be noted that the localization of the eigenfunction and its growth rate is a different matter. The growth rate actually becomes greater with the background magnetic field strength increased, as shown in Figure 1, due to a large gradient of the field.

This localization implies a small B_{x1} compared with the initial B_y , but how it affects the average value of the Maxwell stress is not trivial. The estimate of the efficiency of the angular momentum transport is tightly connected with the non-linear behavior and the problem of the saturation mechanism. In the next section, we will discuss the significant contribution of the present instability to the stress tensor, using non-linear simulations.

3. NONLINEAR SIMULATIONS

This section provides the results of fully-non-linear MHD simulations designed to validate the presence of MGDIs suggested in the previous section and to investigate the non-linear time evolution. Specifically, we focus on the efficiency of angular momentum transport.

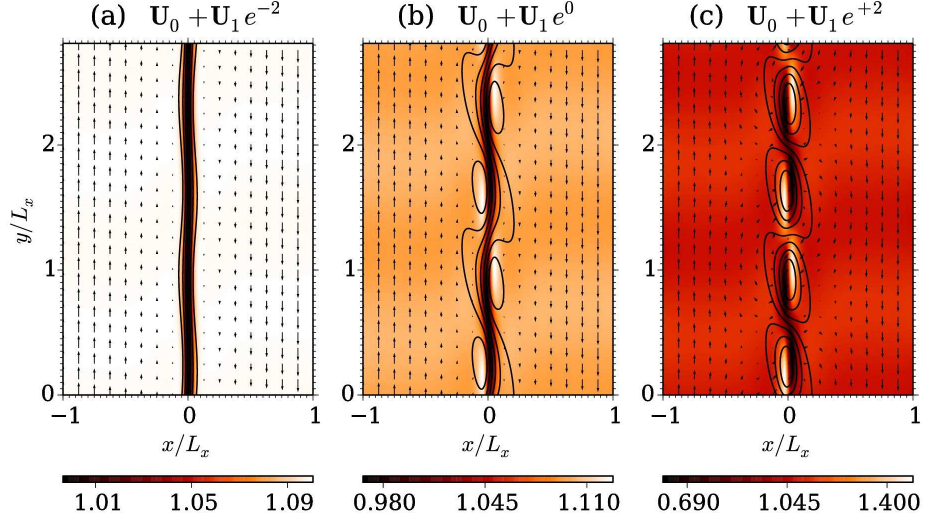


Fig. 5.— Unstable eigenfunction with $\beta = 10$ and $k_y d = 0.223$. The format is same as in Figure 4. The growth rate is 0.430Ω .

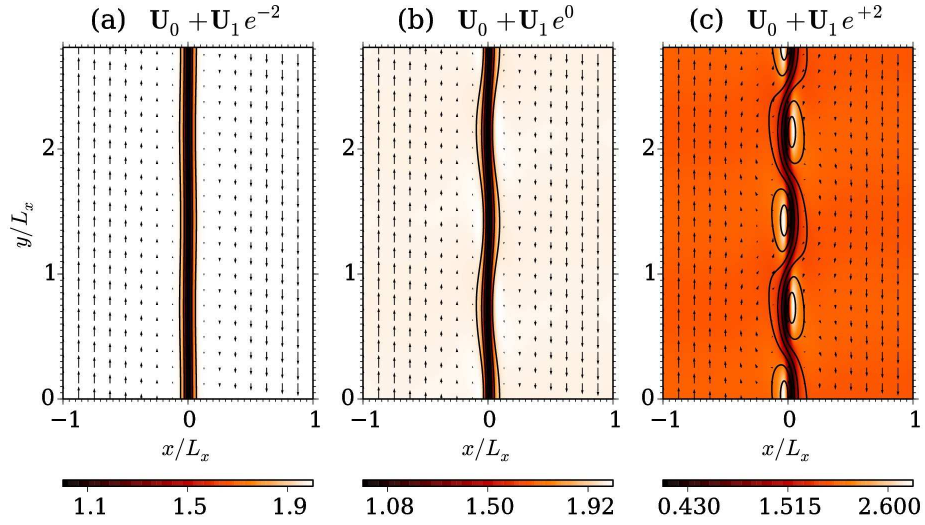


Fig. 6.— Unstable eigenfunction with $\beta = 1$ and $k_y d = 0.223$. The format is same as in Figure 4. The growth rate is 0.675Ω .

3.1. Basic Equations and Simulation Codes

We solve the same equations as used in the previous section, i.e., from equation (1) to (4), but rewritten in the semi-conservative form:

$$\frac{\partial \rho}{\partial t} + \nabla \cdot (\rho \mathbf{v}) = 0, \quad (10)$$

$$\frac{\partial (\rho \mathbf{v})}{\partial t} + \nabla \cdot \left[\rho \mathbf{v} \mathbf{v} + \left(p + \frac{B^2}{2} \right) \mathbf{I} - \mathbf{B} \mathbf{B} \right] = -2\rho \boldsymbol{\Omega} \times \mathbf{v} - 2\rho \Omega x v'_{0y} \hat{\mathbf{e}}_x, \quad (11)$$

$$\frac{\partial \mathbf{B}}{\partial t} = \nabla \times (\mathbf{v} \times \mathbf{B}), \quad (12)$$

$$\frac{\partial e}{\partial t} + \nabla \cdot \left[\left(e + p + \frac{B^2}{2} \right) \mathbf{v} - (\mathbf{v} \cdot \mathbf{B}) \mathbf{B} \right] = -2\rho \Omega x v'_{0y} v_x, \quad (13)$$

where $e = \rho v^2/2 + p/(\gamma - 1) + B^2/2$ is the total energy density, and the other notation is same as in the linear analysis. The specific heat ratio is again set to be $\gamma = 5/3$. All quantities are spatially discretized by using the finite difference approach in a computational domain, $-1 \leq x/L_x \leq 1$ and $0 \leq y/L_y \leq 2\pi$, which is resolved with 200×600 grid points.

We calculate the flux with the help of the HLL approximate Riemann solver (Harten et al. 1983) at the face center, where the primitive variables, i.e., ρ , \mathbf{v} , \mathbf{B} , and p , are evaluated as point values by combining a 5th-order weighted essentially non-oscillatory (WENO) interpolation (Liu et al. 1994; Jiang & Shu 1996) and the monotonicity preserving limiter (Suresh & Huynh 1997). The point-value flux is then converted to the appropriate numerical flux with a 6th-order formula (Shu & Osher 1988). The cell-centered conservative variables are finally updated using the 3rd-order TVD Runge-Kutta method (Shu & Osher 1988). To avoid a spurious magnetic monopole, the HLL-upwind constrained transport (UCT; Londrillo & Del Zanna (2004)) treatment is employed for updating the face-centered magnetic field, in which the edge-centered electric field is evaluated using WENO interpolation and the HLL average. Note that the results to be shown in this section will not largely change, even if the HLLD Riemann solver, which is more accurate than the HLL Riemann solver especially in high- β plasmas (Mignone et al. 2007, 2009), is employed instead. The quantitative behavior of statistics, however, slightly differs due to the higher resolution of each wave mode. In particular, less diffusivity is preferable to larger stress related to turbulent motion in small scales.

3.2. A Single Localized B-Field

Our initial condition is set to be a superposition of exactly the same equilibrium state considered in our linear analysis and a random perturbation of the in-plane velocity, the amplitude of

which is fixed to 1% of the sound speed measured in an unmagnetized region. Without the random perturbation, the system would remain in the initial equilibrium state. To calculate the long time evolution of the system, we implement the standard shearing periodic boundary condition. Even if one adopts a conducting wall boundary, the results do not change in the early stage, before the distorted magnetic fields approach the radial boundary.

From left to right in Figure 7, snapshots of the simulations with $\beta=100$, 10, and 1 taken at time $\Omega t/2\pi = 20$ are shown. The format of each panel is same as in Figures 4 to 6 except for the range of the y -coordinates. All of these cases show the negative correlation between B_x and B_y reflected as the downward-sloping magnetic field lines, which contributes to angular momentum transport. While the linear theory discussed in the previous section predicts broadband growth for a stronger initial field, the typical scale of the bending of the field line is clearly larger for smaller β , which suggests that the magnetic tension force works more efficiently in non-linear evolution and then the growth of short waves is suppressed. In larger β cases, on the other hand, the bent mean structure and other small-scale magnetic structures appear. Such structures first grow along the both sides of the initial field, where the large gradient $|\partial B_y/\partial x|$ exists, and then they are torn off from the mean field by magnetic reconnection. (Note that magnetic reconnection occurs via numerical resistivity, but the non-linear evolution does not change by assuming a finite resistivity.) In any case, the non-linear growth up to torsion of the localized magnetic field is ascertained. Note that the stage where the linear theory is applicable finishes instantly, since the growing perturbed field quickly breaks the background structure of the initial magnetic field.

Figure 8 summarizes the box-averaged stress as a function of time. The xy -components of the Reynolds stress and the Maxwell stress normalized by the initial gas pressure, or the so-called α -parameters, are plotted in each panel. The instantaneous Reynolds stress generally fluctuates significantly with time, but the temporal average over the interval $15 \leq \Omega t/2\pi \leq 20$ takes a positive value of the order of 10^{-3} . The Maxwell stress, on the other hand, remains positive during the non-linear evolution, which is still smaller by one to two orders of magnitude compared with the local three-dimensional simulations of MRIs (Hawley et al. 1995, 1996, etc.). Note that the case of $\beta = 100$ shows a remarkably small value in spite of a more broken structure, due to the weakness of the initial field.

To put it another way, however, once the magnetic field lines are stretched to the point of crossing the radial boundary, much stronger azimuthal fields could be expected. The point is a stretching term in the governing equation for the azimuthal magnetic energy,

$$\frac{d}{dt} \left(\frac{B_y^2}{2} \right) = B_x B_y \frac{\partial v_y}{\partial x} - B_y^2 \frac{\partial v_y}{\partial x}, \quad (14)$$

where the first and the second terms in the right-hand side represent the energy change by stretching and compressive motions, respectively. Especially, the energy increase through the background velocity shear, $B_x B_y v'_{y0}$, is called the Ω -dynamo. In a radially periodic system like the shearing box, if a fluid element moves largely across the radial boundaries, the total velocity shear the

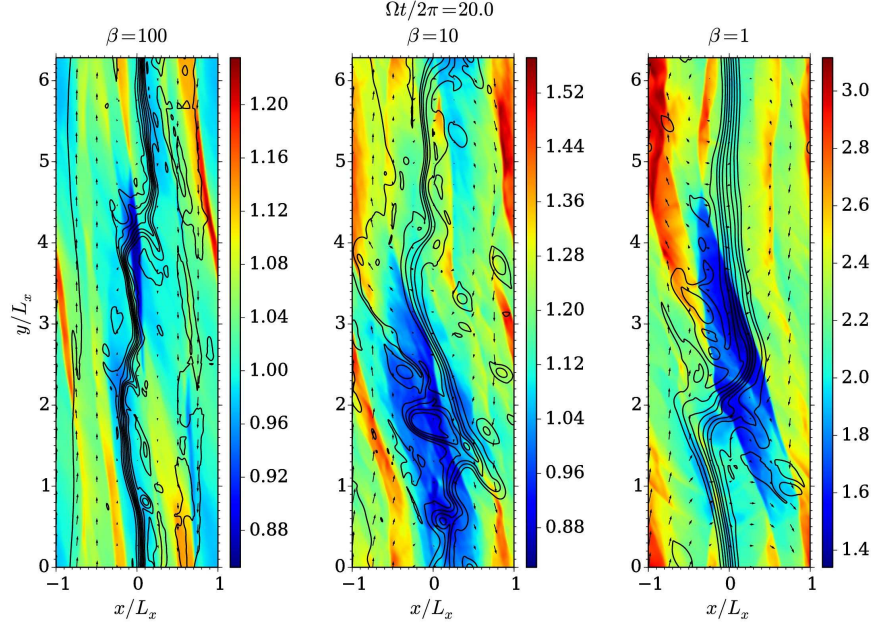


Fig. 7.— Snapshots of the MHD simulations at twenty times the orbital period. The color contours, solid lines, and arrows represent the gas pressure, the lines of magnetic force, and the in-plane velocity, respectively.

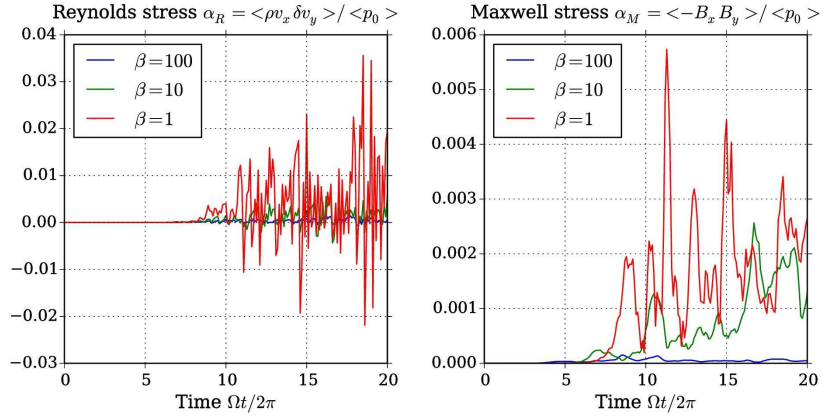


Fig. 8.— Time histories of the box-averaged stress. The left and right panels show the xy -components of the Reynolds stress and the Maxwell stress normalized by the averaged initial gas pressure, that is, the α parameters.

element feels can become much larger than the shear just inside one simulation domain, $q\Omega L_x$. The larger radial fluctuation, therefore, leads to the stronger azimuthal magnetic energy. The next subsection is devoted to suggesting such a possible path leading to a more amplified magnetic field and a resultant large Maxwell stress.

3.3. Multiple Localized B-fields

As a phenomenon expected to occur in accretion disks, let us consider the situation where a toroidal magnetic field has multiple structures rather than a single localized field. The motivation of this idealized setup comes from, for example, the existence of parasitic instabilities occurring on a current sheet, which induce periodic variation of plasma parameters along an equatorial plane (Goodman & Xu 1994; Pessah & Goodman 2009; Rembiasz et al. 2016). The physical mechanism driving the instability in the linear stage does not change even in this case, but a more turbulent state could be expected in the non-linear stage as a result of coupling between neighboring fields. This section shows a possible path through which the MGDIs may contribute to turbulence generation and anomalous angular momentum transport.

The simulation setup is the same as described in the previous subsection except for the initial profile of the magnetic field. Here we assume the functional form of the toroidal magnetic field as follows:

$$B_{y0}(x) = B_c \cos^4\left(\frac{3\pi x}{L_x}\right), \quad (15)$$

which reproduces both the locality within $0.05L_x$ and the periodicity of the localized structure. The pressure and density profiles are also modified to keep dynamical and thermal equilibrium. The plasma beta is defined using the peak value of the magnetic field, B_c , and the gas pressure at the same site.

Figures 9, 10, and 11 show snapshots at characteristic stages in the cases with $\beta=100$, 10, and 1, respectively. The three panels in each figure are taken at times $\Omega t/2\pi=5$, 10, and 20 from left to right, and the format of each panel is the same as in Figure 7. In the leftmost panel in Figure 9, we can see that the discrete magnetic field lines are distorted individually in the early stage by the non-linear growth, just as demonstrated in the simulations with a single localized field. The bending of the field lines grows as time goes on, and before ten orbital periods they drastically overlap and merge with the neighboring magnetic fields. The mixing of the magnetic field is completed by 20 orbital periods, and the simulation domain is filled with a lot of magnetic islands as a result of the repetitive reconnection process. Recall that, in a single channel case, the reconnected field simply gets torn off the background field and shows no further turbulent development. At this stage, the energy contained in the magnetic field increases to about 10% of the kinetic energy of the background differential rotation. Even if the difference of the initial magnetic energy is taken into account, this ratio is rather large compared with the case of a single localized field, where the magnetic energy at the saturated stage is smaller by three orders of magnitude.

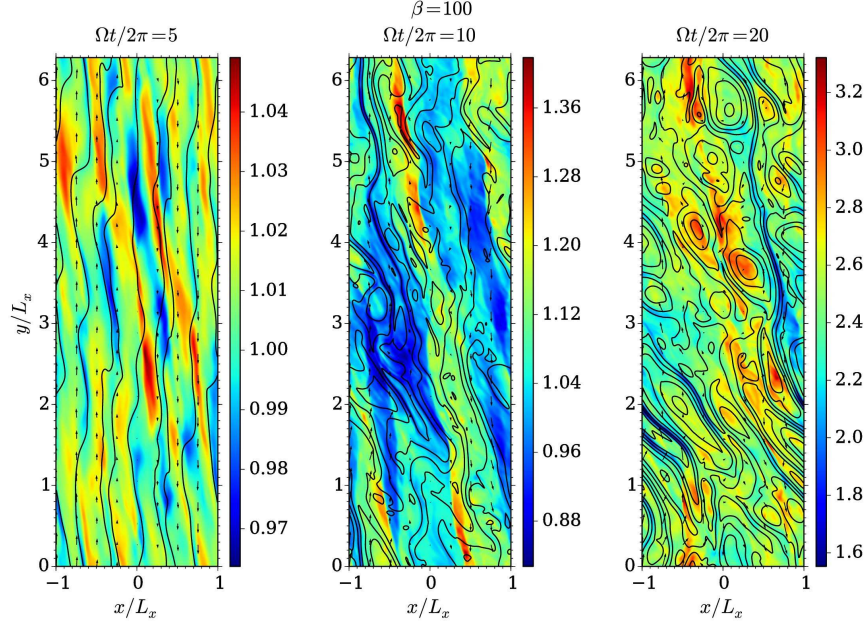


Fig. 9.— Snapshots of the simulation started from a wavy toroidal field with $\beta = 100$, taken at 50, 100, and 200 orbits. The format of each panel is the same as in Figure 7.

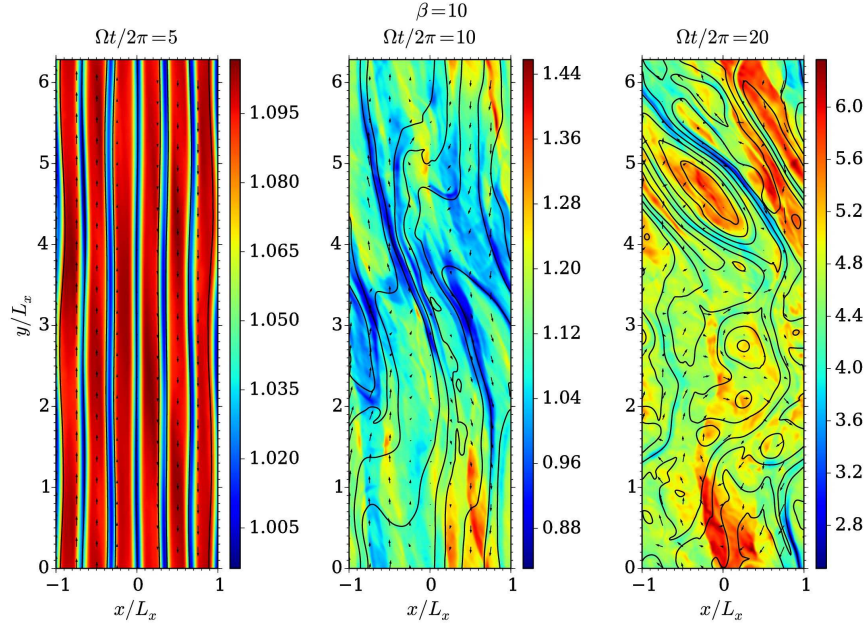


Fig. 10.— Snapshots of the case of $\beta = 10$, with the same format as in Figure 9.

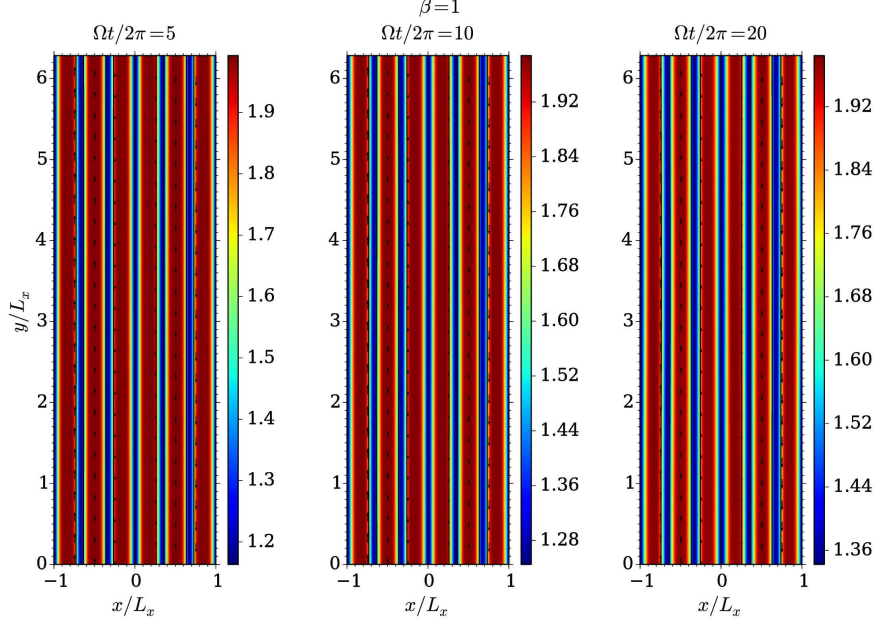


Fig. 11.— Snapshots of the case of $\beta = 1$, with the same format as in Figure 9.

The detailed time history of the box-averaged energy is summarized in Figure 12(a), which shows that the dynamo process works efficiently on both B_x and B_y at an early stage before 20 orbital periods, and roughly speaking, an equipartition is eventually attained between the kinetic energy in the x -direction and the magnetic energy in the x - and y -directions. The production of the strong azimuthal field is understood as a natural consequence from equation (14), which tells the effect of Ω -dynamo. A similar relation holds with regard to the radial field energy as

$$\frac{d}{dt} \left(\frac{B_x^2}{2} \right) = B_x B_y \frac{\partial v_x}{\partial y} - B_x^2 \frac{\partial v_y}{\partial y}, \quad (16)$$

which shows that shear motion in the radial velocity newly generates the radial magnetic field. It is clear that in the MGDI this radial velocity is driven by the magnetic pressure gradient force, while the gravity-related terms play the same role in the case of MRI. In this sense, the dynamo process working here looks quite similar to that in the MRI not only in the azimuthal field, but also in the radial field. At the saturated stage, the gas pressure gradually increases through magnetic reconnection, creating many magnetic islands.

Even when the initial magnetic energy is ten times as large, that is, $\beta = 10$, the same instability grows as shown in Figure 10. Compared with the case of $\beta = 100$, it can be seen that the typical scale of the growing mode becomes larger, as does the size of the magnetic islands in the final stage. The gas pressure at 20 orbital periods increases about twofold, which implies that the total amount of energy input into the system across the boundaries is enhanced and continuously converted to the internal energy of the plasma through magnetic reconnection. In other words, the total stress

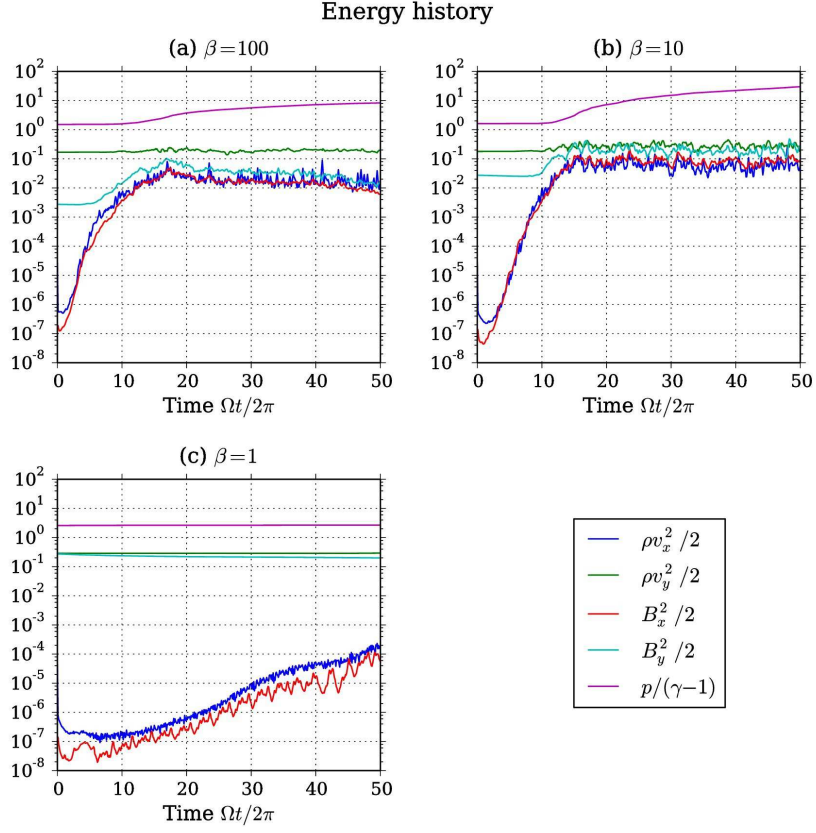


Fig. 12.— Temporal development of the box-averaged energy divided into the contribution from the x and y directions, all of which are normalized by the gas pressure measured in a magnetized region. Each panel shows the results for (a) $\beta = 100$, (b) $\beta = 10$, and (c) $\beta = 1$, respectively.

integrated along the radial boundary gets larger, since the time variation of the total energy, e , can be described as follows:

$$\frac{\partial}{\partial t} \int e dV = 2 |v_{0y}(L_x)| \int_{x=L_x} W_{xy} dy - \int 2\rho\Omega x v'_{0y} v_x dV, \quad (17)$$

where $W_{xy} = \rho v_x \delta v_y - B_x B_y$ is the total stress. The second term on the right-hand side of equation (17), which represents the change in the total gravitational potential in the simulation domain, becomes nearly zero on average. The detailed time history of each energy component is plotted in Figure 12(b). As in the case of $\beta = 100$ shown in panel (a), the growing mode is saturated before 20 orbital periods, after which the kinetic energy related to v_x and the magnetic energy reach a level comparable to the background differential rotation, but slightly larger than those in the case with a weaker initial field.

However, this situation changes significantly for the strong magnetic field with $\beta = 1$ shown in Figure 11. The initial equilibrium state holds and no growing mode can be observed. It is interesting to note that the non-linear evolution is accomplished in the single field case discussed in the previous subsection. The energy history in Figure 12(c) also shows a quite calm variation. The suppression of the growing mode is indeed the result of the non-linear magnetic tension force, since we confirmed the presence of unstable modes in linear analyses under the initial magnetic profile described here.

We summarize the time histories of the Reynolds and Maxwell stresses in Figures 13(a) and 13(b), respectively. The result of $\beta = 1$, denoted by the red line, shows no stress for either the Reynolds or Maxwell components, because the initial equilibrium state is almost conserved. In the cases with $\beta = 10$ and 100, denoted by the green and blue lines, the Reynolds and Maxwell stresses averaged after 20 orbital periods are -0.00109 and 0.0235 for $\beta = 100$, and -0.0164 and 0.126 for $\beta = 10$, respectively. The Maxwell stress, therefore, is larger by about two orders of magnitude than the results in the single field case, which means a qualitative change in the non-linear behavior, rather than the simple quantitative superposition due to an increase in the initial total magnetic flux. In addition, the result for a stronger shear motion with $q = 1.5$, which corresponds to the Kepler rotation, is also plotted as a cyan line. The basic mechanism driving the instability is same as in the case with $q = 1.0$, but thanks to the more powerful Ω -dynamo effect, the MGDl can grow more quickly non-linearly and a larger Maxwell stress can be attained at the saturated stage.

The β -dependence of the Maxwell stress averaged during the saturated stage between $30 \leq \Omega t/2\pi \leq 50$ is summarized in Figure 14. It can be clearly seen that the results are well fitted by a power law of $\beta^{-1/2}$ as long as $\beta > 2$, which indicates the proportionality to the initial magnetic flux rather than magnetic energy density, while the cases starting with $\beta < 2$ result in almost no stress.

The suppression of instabilities for a small β is highly relevant to the large characteristic spatial scale under the strong magnetic tension force, which works less efficiently for longer waves. Although

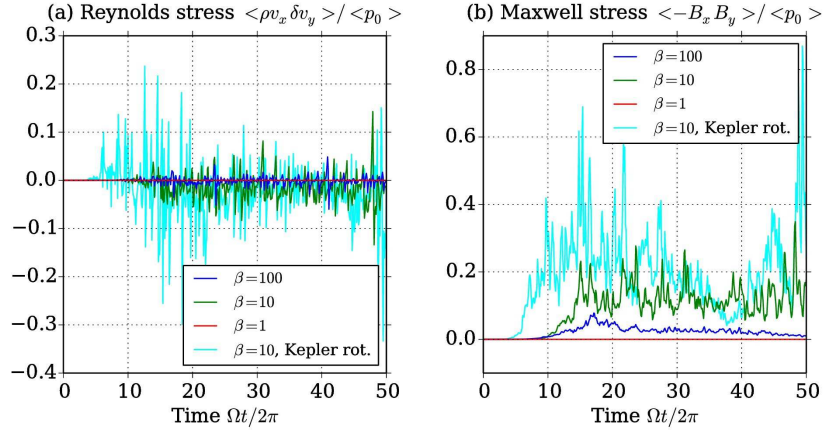


Fig. 13.— The xy -components of the (a) Reynolds and (b) Maxwell stress tensors as functions of time.

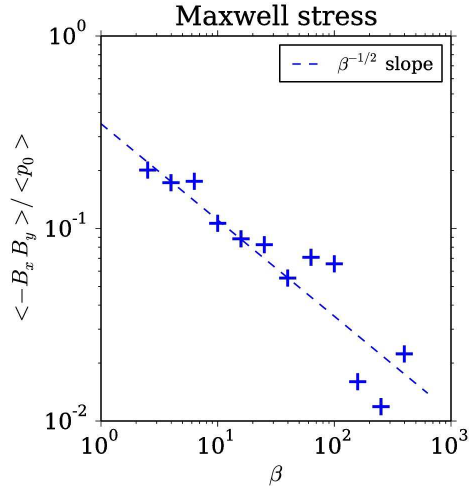


Fig. 14.— The Maxwell stress averaged during the saturated stage as a function of the initial β .

this mode has a broad unstable range in wavelength with respect to the linear theory around a single channel, the nonlinear growth is actually quenched in the multiple channel case. Once the simulation box is extended double in the azimuthal direction, however, the drastic growth in the Maxwell stress via channel merging process is activated even for $\beta = 1$. This certainly happens because the extended box allows the growth of the fluctuations with the scale larger than the original domain size. Figure 15 shows the time histories of the Reynolds and Maxwell stress for $\beta=1, 10$, and 100 , respectively, normalized by the volume averages of the instantaneous thermal pressure, $\langle p(t) \rangle$. From the right panel, we can clearly observe the enhancement of the Maxwell stress by the nonlinear growth after 50 orbits for $\beta = 1$. Except for the shifted time this drastic merging is switched on, the statistical behavior is quite similar in all cases, which implies that the MGDI works as the common underlying mechanism to drive the turbulence.

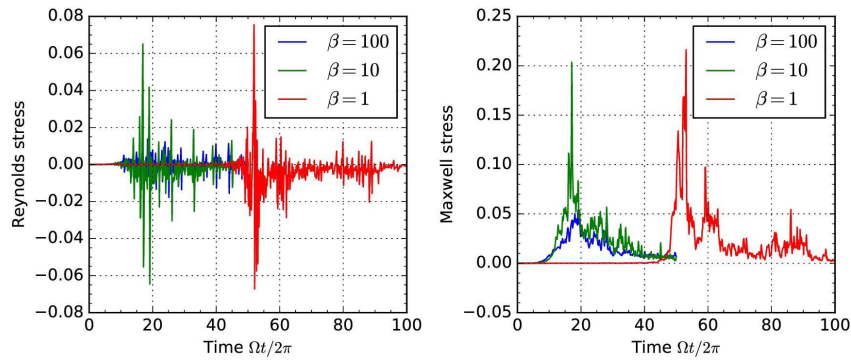


Fig. 15.— Time histories of the Reynolds and Maxwell stress normalized box averages of the instantaneous gas pressure in the elongated simulation box, $(x, y) \in (2L_x, 4\pi L_x)$, for different initial β .

4. SUMMARY AND CONCLUSION

In the present paper, we have proposed a new plasma instability, MGDI, which can generate a highly turbulent state in an accretion disk and contribute to the enhanced transport of angular momentum. Driven by the spatial non-uniformity of a toroidal magnetic field, an unstable mode completely confined within the equatorial plane can be realized, in contrast to the previous studies on the toroidal MRI, in which a vertical wavenumber always dominates over a finite azimuthal component.

The growth rates and eigenfunctions of this instability are calculated by linear eigenvalue analysis, and the corresponding non-linear evolution is then demonstrated using two-dimensional MHD simulations. While the simulations beginning with a single localized toroidal field reveal the non-linear growth of the MGDI, it is shown that the angular momentum transport does not

work so efficiently in the saturated stage. If the instabilities occur in the neighboring field lines under the multiple localized magnetic fields rather than in an isolated situation, however, they drastically overlap with each other and a well-developed turbulent state can be realized. In such a case dynamo action by differential rotation begins to work efficiently on magnetic field lines crossing the radial boundaries, which contributes to a large Maxwell stress. Furthermore, we have shown that a toroidal field with a larger magnetic flux is favorable for the Maxwell stress to reach a large value, but this drastic transition does not occur for a magnetic field that is too strong with $\beta < 2$, as long as we employ the box size $(x, y) \in (2L_x, 2\pi L_x)$. Once the simulation domain is elongated, the transition is reactivated, but it takes much longer time to switch on the drastic merging. It is worth noting that the situation with $1 \leq \beta \leq 10$, which is favorable to the growth of the MGDI, often appears during a non-linear phase in a local simulation of the MRI for a relatively small initial beta, $\beta \sim \mathcal{O}(10^2)$. In the cases with larger initial β values, like $\beta \sim \mathcal{O}(10^{3-6})$, the final states still seem to be in the unstable regime (e.g., Hawley et al. 1995; Sharma et al. 2006; Minoshima et al. 2015).

Although the profile of the toroidal magnetic field discussed here is one of the most idealized situations, the physical essence to drive the instability does not change even under a different structure, as long as an enough radial gradient of the magnetic field is available. There is, therefore, possibility that the present unstable mode will arise around various kinds of fluctuation in the toroidal field, like via parasitic modes including the Kelvin-Helmholtz instability and the tearing instability.

It should be emphasized again that the efficiency of the angular momentum transport obtained here is comparable to that obtained in evaluation in three-dimensional simulations of MRIs assuming an initial toroidal field, in spite of the low dimensionality, and therefore, the MGDI is capable of driving strong turbulence alone. One might expect not just the sole contribution, but also coupling with magnetic reconnection occurring parallel to the equatorial plane during the nonlinear phase of MRI, and with the toroidal MRIs as considered in previous studies if vertical variation is also taken into account. It is still not obvious that how large contribution the instabilities have in fully three-dimensional shearing boxes. Nevertheless, since they provide new paths toward turbulence without any finite k_z in contrast to the conventional toroidal MRIs, the complementary growth between toroidally and vertically propagating waves, rather than competitive growth, should be expected. The present instability could possess the ability to play a wide variety of crucial roles in the mechanism of turbulence generation in differentially rotating systems.

We thank T. Amano and T. Saito for their useful discussion. This work was supported by JSPS KAKENHI Grant Number 26-394.

REFERENCES

Bai, X-N. 2015, ApJ, 798, 84

- Balbus, S. A., & Hawley, J. F. 1991, *ApJ*, 376, 214
- Balbus, S. A., & Hawley, J. F. 1992, *ApJ*, 400, 610
- Balbus, S. A., & Hawley, J. F. 1998, *Rev. Mod. Phys.*, 70, 1
- Balsara, D., & Spicer, D. S. 1999, *J. Comp. Phys.*, 149, 270
- Blandford, R. D., & Payne, D. G. 1982, *MNRAS*, 199, 883
- Borges, R., Carmona, M., Costa, B., & Don, W. S. 2008, *J. Comp. Phys.*, 227, 3191
- Cannizzo, J. K., Shafter, A. W., & Wheeler, J. C. 1988, *ApJ*, 333, 227
- Fragile, P. C., & Blaes, O. M. 2008, *ApJ*, 687, 757
- Goodman, J., & Xu, G. 1994, *ApJ*, 432, 213
- Harten, A., Lax, P. D., & van Leer, B. 1983, *SIAM Rev.*, 25, 35
- Hawley, J. F., Gammie, C. F., & Balbus, S. A. 1995, *ApJ*, 440, 742
- Hawley, J. F., Gammie, C. F., & Balbus, S. A. 1996, *ApJ*, 464, 690
- Hoshino, M. 2015, *Phys. Rev. Lett.*, 114, 6
- Jiang, G. S., & Shu, C-W. 1996, *J. Comp. Phys.*, 126, 202
- Kunz, M. W., & Lesur, G. 2013, *MNRAS*, 434, 2295
- Liu, X-D., Osher, S., & Chan, T. 1994, *J. Comp. Phys.*, 115, 200
- Londrillo, P., & Del Zanna, L. 2004, *J. Comp. Phys.*, 195, 1
- Matsumoto, R., & Tajima, T. 1995, *ApJ*, 445, 767
- Mignone, A., Bodo, G., Massaglia, S., Matsakos, T., Tesileanu, O., Zanni, C., & Ferrari, A. 2007, *ApJS*, 170, 228
- Mignone, A., Ugliano, M., & Bodo, G. 2009, *MNRAS*, 393, 1141
- Mignone, A., Rossi, P., Bodo, G., Ferrari, A., & Massaglia, S. 2010, *MNRAS*, 402, 7
- Minoshima, T., Hirose, S., & Sano, T. 2015, *ApJ*, 808, 54
- Mizuno, Y., Hardee, P. E., & Nishikawa, K. I. 2014, *ApJ*, 784, 167
- O’Neill, S. M., Beckwith, K., & Begelman, M. C. 2012, *MNRAS*, 422, 1436
- Papaloizou, J. C. B., & Pringle, J. E. 1984, *MNRAS*, 208, 721

- Pessah, M., & Goodman, J. 2009, *ApJ*, 698, 72
- Rembiasz, T., Obergaulinger, M., Cerdá-Durá, P., Müller, E., & Aloy, M. A. 2016, *MNRAS*, 456, 3782
- Sano, T., & Inutsuka, S. 2001, *ApJ*, 561, 179
- Sano, T., & Stone, J. M. 2002, *ApJ*, 570, 314
- Shakura, N. I., & Sunyaev, R. A. 1973, *A&A*, 24, 337
- Sharma P., Hammett, G. W., Quataert, E., & Stone, J. M. 2006 *ApJ*, 637, 952
- Shu, C-W., & Osher, S. 1988, *J. Comp. Phys.*, 77, 439
- Simon, J. B., Beckwith, K., & Armitage, P. J. 2012, *MNRAS*, 442, 2685
- Simon, J. B., & Hawley, J. H. 2009, *ApJ*, 707, 833
- Stone, J. M., & Gardiner, T. A. 2010, *ApJS*, 189, 142
- Stone, J. M., Hawley, J. F., Gammie, C. F., & Balbus, S. A. 1996, *ApJ*, 463, 656
- Stone, J. M., & Norman, M. L. 1994, *ApJ*, 433, 746
- Suresh, A., & Huynh, H. T. 1997, *J. Comp. Phys.*, 136, 83
- Zhu, Z., Stone, J. M., & Bai, X-N. 2015, *ApJ*, 801, 81